

Holographic Intelligence Surface Assisted Integrated Sensing and Communication

Zhuoyang Liu, Graduated Student Member, IEEE, Yuchen Zhang, Graduated Student Member, IEEE, Haiyang Zhang, Member, IEEE, Feng Xu, Senior Member, IEEE, and Yonina C. Eldar, Fellow, IEEE

Abstract—Traditional discrete-array-based systems fail to fully exploit interactions between closely spaced antennas, resulting in inadequate utilization of the aperture resource. In this paper, we propose a holographic intelligence surface (HIS) assisted integrated sensing and communication (HISAC) system, wherein both the transmitter and receiver are fabricated using a continuous-aperture array. To enable tractable design and optimization, we introduce a Fourier-based continuous-discrete transformation, converting the continuous pattern design into a finite-dimensional representation in the wavenumber domain. Based on this transformation, we formulate a joint transmit–receive beamforming optimization problem that aims to maximize multi-target sensing performance while satisfying multi-user communication requirements. To solve the non-convex problem with coupled variables, an alternating optimization-based algorithm is proposed to optimize the HISAC transmit–receive beamforming in an alternate manner. Specifically, the transmit beamforming design is solved by decoupling into a series of feasibility-checking sub-problems while the receive beamforming is determined by the Rayleigh quotient-based method. Simulation results demonstrate the superiority of the proposed HISAC system over traditional discrete-array-based ISAC systems, achieving significantly higher sensing performance while guaranteeing predetermined communication performance.

Index Terms—Holographic intelligence surface, integrated sensing and communication, pattern design strategy, continuous-aperture array

I. Introduction

Integrated sensing and communication (ISAC) system, which envisions simultaneous sensing and communication on a shared waveform/platform, is considered a vital solution for tackling challenges associated with spectral and/or power efficiency in 6G wireless networks [1], [2]. In a multi-antenna setting, joint ISAC waveform design is typically achieved through transmit beamforming design. This entails designing spatial beamformers judiciously to maximize sensing/communication under performance constraints in communication/sensing, thereby striking a balance between the two functionalities [3]–[5]. Furthermore, by leveraging radar receivers, joint transmit–receive beamforming has been proposed in the literature to further enhance ISAC performance [6]–[8].

Z. Liu and F. Xu are with the Key Lab for Information Science of Electromagnetic Wave (MoE), Fudan University, Shanghai 200433, China (e-mail: {liuzy20; fengxu}@fudan.edu.cn).

Y. Zhang is with the National Key Laboratory of Wireless Communications, University of Electronic Science and Technology of China, Chengdu 611731, China (e-mail: yc_zhang@std.uestc.edu.cn).

H. Zhang is with the School of Communication and Information Engineering, Nanjing University of Posts and Telecommunications, Nanjing 210003, China (e-mail: haiyang.zhang@njupt.edu.cn).

Y. C. Eldar is with the Faculty of Math and CS, Weizmann Institute of Science, Rehovot 7610001, Israel (e-mail: yonina.eldar@weizmann.ac.il).

The aforementioned beamforming designs in ISAC systems typically rely on discrete antenna arrays, where the antenna spacing is constrained to half-wavelength. This limits the number of antennas for a given aperture, thereby resulting in insufficient exploitation of array gain for ISAC performance enhancement [9], [10]. In addition, modeling electromagnetic (EM) propagation for the discrete array usually overlooks the mutual interference between two closely spaced antennas, potentially leading to inadequate information acquisition during signal reception [11], [12]. To overcome these limitations, the concept of holographic intelligence surface (HIS), also as known as holographic multiple-input multiple-output (MIMO) [13], [14] and continuous-aperture MIMO [15], [16], has emerged. By forming an effectively continuous-aperture, HIS enables more complete utilization of the physical aperture of the antenna array, thereby maximizing the radiated energy in the desired direction and approaching the aperture-limited directivity. Unlike the discrete array consisting of multiple patch antennas with half-wavelength spacing, HIS achieves a quasi-continuous-aperture array by deploying massive sub-wavelength tunable elements in a compact space [17]. This architecture mitigates the element-spacing constraints inherent in discrete arrays, enabling higher array gain for the same physical aperture size [10], [18]. The advantages of HIS include enhancing signal coverage [19], improving communication rate [20], and boosting localization accuracy [10], [21]. However, due to its continuous nature, HIS incurs significant challenges for array signal processing, making traditional beamforming techniques [3]–[8], which are tailored for discrete arrays, inefficient or even inapplicable [13], [14]. Due to these challenges, integrating HIS into the ISAC system, though promising for achieving a better performance trade-off between sensing and communication, is still in its infancy.

The primary goals of this work are to: 1) design an HIS-assisted ISAC (HISAC) transceiver architecture, 2) develop an HISAC transmit–receive beamforming framework, and 3) demonstrate the performance gain by employing HIS instead of traditional discrete arrays in ISAC systems.

A. Prior work

Many efforts have been dedicated to beamforming design for the ISAC systems [3]–[8], [22]–[24], including transmit beamforming and joint transmit–receive beamforming. Transmit beamforming builds on the spatial degrees of freedom (DoFs) at the transmitter, which is devised to strike performance trade-off between sensing and communication [3]–[5]. A commonly adopted strategy

TABLE I
Summary Comparison of Related HIS / Holographic Systems

Work	Aperture Model	System Scope	Control Variables
Holographic MIMO [26]	Discrete (element-level)	Localization	Phase shifts of RHS elements
Circular Holographic MIMO [27]	Discrete (element-level)	Comm. / Throughput	Phase shifts of RHS elements
Overview of RHSs [28]	Discrete (element-level)	ISAC	Amplitude and phase of RHS elements
Shape-adaptive RHSs [29]	Discrete (element-level)	Comm. / Throughput	Amplitude, phase, and geometry parameters
RHS-assisted ISAC [17], [30]	Discrete (element-level)	ISAC	Amplitude and phase of RHS elements
Continuous-aperture HIS [16], [31]	Continuous	Comm. / Throughput	EM-consistent surface patterns
This work	Continuous	ISAC	Wavenumber-domain coefficients

Note: Holographic MIMO, reconfigurable holographic surfaces (RHSs), and HISs denote related surface-based architectures. In particular, discrete-aperture HMIMO/RHS systems correspond to element-level control of amplitude and phase, whereas continuous-aperture HIS models rely on continuous electromagnetic representations or equivalent wavenumber-domain coefficients.

Abbreviations: Comm. : Communication.

of transmit beamforming is to modify the transmit beam by optimizing the beamformer, aiming to maximize the power sent towards the targets while fulfilling the communication performance requirement at each user [3]–[5].

Transmit beamforming fails to explore the spatial DoFs at the radar receiver, which holds potential to further enhance ISAC performance. Joint transmit-receive beamforming, in which the transmitter-side beamformers and radar receiver-side beamformers/filters are designed simultaneously, has been proposed in [6]–[8], [22]–[25]. In [22], the authors considered transmit-receive beamforming in ISAC systems with signal-to-interference-and-noise ratio (SINR) being the radar performance metric. However, without being optimized adaptively, the receive beamforming conducted at the radar receiver was solely determined by the steering vector. As a step further, [25] proposed a design framework for ISAC transmit-receive beamforming, optimizing transmit and receive beamformers alternately. The aforementioned works regarding ISAC beamforming typically rely on a discrete array, which limits performance due to inefficient utilization of a given aperture [11], [12].

With the development of continuous-aperture array technology, HIS has been devised to alleviate the performance bottleneck caused by traditional discrete arrays, enabling higher array gain for a given aperture size [9]–[14]. The superiority of HIS has been demonstrated in various systems aimed at different tasks, including communication, localization, and other integrated services [17], [26]–[30], [32], [33]. Existing holographic systems are predominantly modeled using sub-wavenumber discrete dipole representations to approximate quasi-continuous distributions [17], [26]–[30]. Such formulations have been widely adopted for communication-centric designs [26], [27], [29] and ISAC systems [17], [30], as summarized in Table I. In particular, [29] adopts a discrete element-level model and focuses on optimizing surface geometry and phase shifts for communication-oriented performance. By contrast, continuous-aperture HIS models describe the surface using continuous electromagnetic fields, which provide a more fundamental characterization of the spatial DoF.

To characterize the radiation model of HIS, it is neces-

sary to design the surface pattern, known as the current density distribution, for a continuous-aperture array [13]–[16]. The authors of [34], [35] modeled the radiation of continuous-aperture arrays and derived a closed-form expression of the capacity between two continuous volumes by utilizing the Fourier basis functions of continuous-space EM channels. To optimize the capacity of HIS-based communications, a pattern division multiplexing (PDM) method was developed to model the radiation for HIS [16], aiming to maximize the sum rate of multi-users with HIS.

B. Motivation and Contribution

Table I provides a high-level comparison of representative discrete-array, holographic, and HIS-based systems. Most existing works employing HIS have focused on communication tasks [31], whereas the incorporation of HIS into ISAC systems has remained in its infancy [17], [30]. Although the advantages of deploying sub-half-wavelength-spacing antennas for ISAC systems have been initially revealed in [17], [30], the advocated antenna array remained discrete. Therefore, the proposed schemes are not applicable to HISAC systems comprised of continuous-aperture arrays.

To fill the gap, this work focuses on incorporating HIS into ISAC systems. Specifically, we propose an ISAC transceiver structure based on HIS, in which both the transmitter and receiver at the base station (BS) are implemented using continuous-aperture HISs. By generating a specific pattern of the HIS, the radiation of the EM waves can be configured to support multi-target sensing and multi-user communication simultaneously. However, due to its continuity, the pattern of the HIS has infinite dimensions, posing significant computational challenges. To address this, we develop a continuous-discrete transformation based on the Fourier series, which maps the spatial-domain current into a finite-dimensional representation in the wavenumber domain. Compared to [16], [34], we further derive a closed-form expression for the far-field Green’s function in the Fourier domain, which enables precise SINR evaluation. This allows the original pattern design to be reformulated as a joint transmit-receive beamforming, where the beamforming matrices in

the wavenumber domain are optimized to configure the radiation beams of the HIS. We then jointly optimize the transmit-receive beamformers to maximize the minimum sensing SINR across multiple radar targets, while ensuring that communication SINR requirements for all users are satisfied.

The main contributions of this work are summarized as follows:

- **HISAC Transceiver:** To the best of our knowledge, we are the first to propose the HISAC system, where the transmit HIS supports multi-user communication and illuminates multiple radar targets, and the receive HIS collects the radar echoes. Specifically, we study the joint design of transmit HIS and receive HIS, balancing the performance of sensing and communication in the proposed system.
- **Fourier-Domain Modeling of Continuous HIS Apertures:** We propose a physically consistent Fourier-domain transformation that maps the continuous surface current distribution of a HIS into a finite-dimensional representation in the wavenumber domain. This leads to an equivalent steering vector expression for continuous-apertures, enabling direct alignment between HIS-based ISAC systems and conventional discrete-array models.
- **Discrete-Compatible Reformulation of the HISAC Problem:** Leveraging the equivalent representation, we reformulate the originally infinite-dimensional beamforming problem into a finite-dimensional structure. The resulting optimization problem shares a similar mathematical form to those for discrete-array ISAC systems, which allows the direct application of existing optimization techniques. To support this formulation, we derive a closed-form expression for the Fourier transform of the far-field Green's function, facilitating precise SINR evaluation in the HISAC problem.
- **Joint Transmit-Receive Beamforming in HISAC:** We develop an alternating optimization (AO) algorithm by recasting the original problem into: transmit HIS design and receive HIS configuration. Due to the high complexity of the involved semidefinite relaxation (SDR)-based method, we propose an adaptive bisection searching (ABS) method to accelerate the convergence in the iteration process. To address the receive HIS configuration, a Rayleigh quotient-based method is proposed to obtain a closed-form solution.

C. Organization and Notation

The rest of the paper is organized as follows: Section II introduces the HISAC system and formulates the pattern design problem. Section III presents the continuous-discrete transformation and reformulates the problem as a joint transmit-receive beamforming design. Section IV describes the proposed optimization methods, and Section V provides numerical results. Finally, Section VI concludes the paper.

Throughout the paper, bold lowercase and uppercase letters denote vectors and matrices, respectively. Notations include $\lambda_{\max}(\mathbf{A})$ for the largest eigenvalue, $\|\cdot\|_2$ and $\|\cdot\|_F$ for the ℓ_2 and Frobenius norms, $(\cdot)^*$, $(\cdot)^T$, and $(\cdot)^H$ for complex conjugate, transpose, and Hermitian, respectively, and $\mathbf{E}(\cdot)$ for expectation. The identity matrix of size N is denoted by \mathbf{I}_N .

II. System Model and problem formulation

A. HISAC Transceiver Architecture

As shown in Fig. 1, we consider multi-user communication and multi-target sensing with the assistance of HISs. We introduce an HISAC system consisting of a transmit HIS \mathcal{P}_S and a receive HIS \mathcal{P}_R . The aperture size for both HISs is $A_T = L_x L_y$, where L_x and L_y are the lengths along x -axis and y -axis, respectively. Specifically,

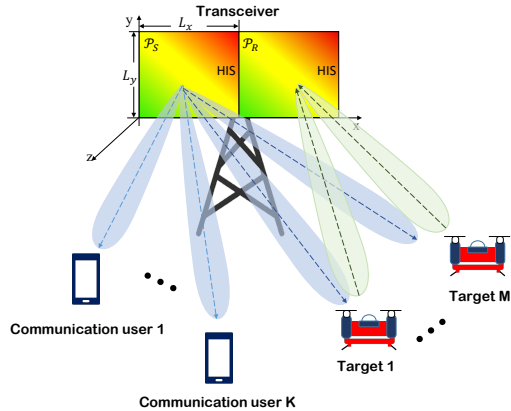


Fig. 1. The illustration of the HIS-assisted integrated sensing and communication system.

\mathcal{P}_S sends signals to perform multi-target sensing and communicate to K single-antenna users simultaneously, while \mathcal{P}_R receives the radar echoes from M targets. The structure of the HISAC transceiver operation is depicted in Fig. 2. The proposed HIS incorporates a single feed directly connected to the radio frequency (RF) distribution network within the surface. The traveling wave originates from the input port, propagates outward along the feed path, and excites the corresponding radiated wave [36]. By carefully designing the surface current distribution $j(p)$, the radiation characteristics $\psi_{\text{rad}}(p)$ can be flexibly controlled, enabling the desired EM environment for ISAC applications. Motivated by this capability, we propose to modulate both the communication data and sensing streams into the surface current pattern of the HIS. Specifically, the communication data streams and sensing streams are modulated into the transmit pattern at \mathcal{P}_S . Similarly, the echoed signals from M targets are received by \mathcal{P}_R , and then demodulated by M receive patterns.

Let $\mathbf{x} = [\mathbf{c}^T, \mathbf{s}^T]^T$, where $\mathbf{c} = [c_1, \dots, c_K]^T \sim \mathcal{CN}(0, \mathbf{I}_K)$ and $\mathbf{s} = [s_1, \dots, s_M]^T$ are communication data streams and sensing streams, respectively. In particular, the sensing signal sequence \mathbf{s} is assumed to have unit power and be uncorrelated with other streams, which is generated by random phase coding [3]. Correspondingly, the transmit

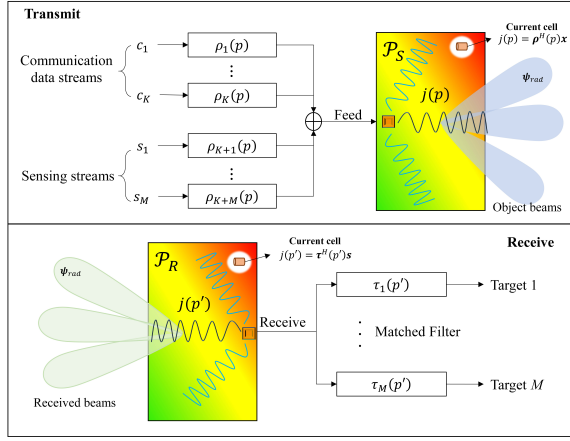


Fig. 2. Illustration of the proposed HISAC transceiver structure.

pattern at point p of the surface is defined as $\boldsymbol{\rho}(p) = [\rho_1, \dots, \rho_{K+M}]^H$. The pattern generated by the communication data streams is given by $j_c(p) = \sum_{k=1}^K c_k \rho_k(p)$ [16]. Similarly, the pattern generated by the sensing streams is given as $j_r(p) = \sum_{m=1}^M s_m \rho_{K+m}(p)$. The combined pattern at \mathcal{P}_S is given by

$$j(p) = \sum_{k=1}^K c_k \rho_k(p) + \sum_{m=1}^M s_m \rho_{K+m}(p) = \boldsymbol{\rho}^H(p) \boldsymbol{x}. \quad (1)$$

As shown in Fig. 2, by exciting each current cell at \mathcal{P}_S with the modulated current $j(p) = \boldsymbol{\rho}^H(p) \boldsymbol{x}$, the ISAC signal is embedded into the HIS and subsequently radiated.

Similar to the transmit end, the received signal is filtered by a set of receive patterns $\boldsymbol{\tau} = [\tau_1, \dots, \tau_M]^H$ at \mathcal{P}_R to extract the target information. Each receive current cell $j(p') = \boldsymbol{\tau}^H(p') \boldsymbol{s}$ is designed to match the specific target, enabling accurate separation and generating the receive beams.

To fully exploit the reconfigurability of the HIS and maximize system performance, both $\boldsymbol{\rho}$ and $\boldsymbol{\tau}$ are jointly optimized to simultaneously improve sensing accuracy and increase communication capacity. In the following, we consider SINR as the performance metric of both communication and sensing, described as follows.

B. Communications and Radar Performances

Let $G_k(p) \triangleq G(p'_k, p)$ be the Green's function from the source p to the user k . Based on the principle of EM propagation theory, the electric field in the space domain is determined by $\boldsymbol{\rho}$ over surface D . The received signal at user k can be calculated by [34]

$$e_k = j\kappa Z_0 \int_D G_k(p) \rho_k(p) c_k dp + \sum_{i=1, i \neq k}^{K+M} j\kappa Z_0 \int_D G_k(p) \rho_i(p) x_i dp + v_c, \quad k = 1, \dots, K, \quad (2)$$

where v_c is the additive white Gaussian noise (AWGN) with variance σ_c^2 , κ is the wavenumber, and Z_0 is the

wave impedance in the free space. The communications SINR of the k -th user, for $k = 1, \dots, K$, is given by

$$\eta_c(\boldsymbol{\rho}; k) = \frac{\mathbf{E} \left(\left| j\kappa Z_0 \int_D G_k(p) \rho_k(p) c_k dp \right|^2 \right)}{\mathbf{E} \left(\left| \sum_{i=1, i \neq k}^{K+M} j\kappa Z_0 \int_D G_k(p) \rho_i(p) x_i dp \right|^2 \right) + \sigma_c^2}, \quad (3)$$

In our considered HISAC system, both communication data streams and radar streams are utilized to support multi-target sensing since they are known by the \mathcal{P}_R from prior sensing steps. In particular, we consider sensing SINR to design a focused HIS beampattern toward regions of interest identified in a previous sensing stage, thereby enabling more refined sensing tasks. Following the standard full-duplex ISAC assumption [1]–[4], [23], self-interference (SI) after cancellation is assumed to be below the noise floor and is therefore omitted [37], [38]. Considering both transmit and receive patterns, the sensing SINR is formulated in the following.

Let $G_m(p) \triangleq G(p'_m, p)$ and $G_m^*(p) \triangleq G(p, p'_m)$ denote the Green's function from source p to m -th targets and from the m -th targets to source p , respectively. The m -th target's echo at p' is expressed as

$$y_m(p') = \alpha_m G_m^*(p) e_m, \quad m = 1, \dots, M, \quad p' \in \mathcal{P}_R, \quad (4)$$

where $e_m = j\kappa Z_0 \int_D G_m(p) \boldsymbol{\rho}(p) \boldsymbol{x} dp$, and α_m is the backscattering intensity of the m -th target. For ease of presentation and without loss of generality, each target's backscattering intensity is considered the same and ignored in the following.

Similarly, the received field at \mathcal{P}_R is determined by $\boldsymbol{\tau}$ over surface D . Then, the received signal with respect to the l -th target is given by

$$y_l = \sum_{m=1}^M \int_D \tau_l(p') y_m(p') dp' + \int_D \tau_l(p') v_r(p') dp', \quad (5)$$

where $v_r(p')$, $p' \in D$ is the AWGN at \mathcal{P}_R with variance σ_r^2 . Therefore, for $l = 1, \dots, M$, the sensing SINR is given by

$$\eta_r(\boldsymbol{\rho}, \boldsymbol{\tau}; l) = \frac{\mathbf{E} \left(\left| e_l \int_D \tau_l(p') G_l^*(p) dp' \right|^2 \right)}{\mathbf{E} \left(\left| \sum_{m=1, m \neq l}^M e_m \int_D \tau_l(p') G_m^*(p) dp' \right|^2 \right) + \sigma_r^2}. \quad (6)$$

C. Problem Formulation in Continuous Domain

From (3) and (6), both the sensing and communication SINRs rely on $\boldsymbol{\rho}$. Meanwhile, the sensing SINR is affected by $\boldsymbol{\tau}$. Here, we aim to strike a performance trade-off between sensing and communication in the proposed HISAC system. Specifically, we propose to maximize the minimal sensing SINR among multiple targets while guaranteeing the multi-user communication SINR requirement. The resulting problem w.r.t. the continuous pattern design is

formulated as

$$\max_{\boldsymbol{\rho}, \boldsymbol{\tau}} \min_{l=1, \dots, M} \eta_r(\boldsymbol{\rho}, \boldsymbol{\tau}; l), \quad (7a)$$

$$\text{s.t. } \eta_c(\boldsymbol{\rho}; k) \geq \Gamma_c, \quad k = 1, \dots, K, \quad (7b)$$

$$\int_D \|\boldsymbol{\rho}\|_2^2 dp \leq P_T, \quad (7c)$$

$$\int_D |\tau_l|^2 dp' = 1, \quad l = 1, \dots, M. \quad (7d)$$

The primary goal of (7) is to balance the sensing SINR among radar targets, and (7b) is the communication constraint for multiple users, where Γ_c represents the minimal required communication SINR. Concerning power constraints, (7c) and (7d) represent the power budget for the transmit pattern at \mathcal{P}_S and the unit-power constraint for the receive pattern at \mathcal{P}_R , respectively. Generally, the receive beamformer's power in the direction of interest is maintained at 1 to ensure a distortionless response for the signal coming from that specific direction, where receive beamforming vectors satisfy $|\tau_l|^2 dp' = 1$.

Due to the presence of infinite-dimensional integrals in both the objective and constraints of problem (7), classical beamforming techniques designed for discrete-array-based ISAC systems are not directly applicable. Moreover, as illustrated in Fig. 2, individually designing each current cell on the HIS surface is impractical from a hardware perspective, motivating the need for a more feasible alternative. To address the challenges posed by the infinite-dimensional functions in problem (7), we develop a continuous-discrete transformation inspired by the Fourier transform and propose a tractable hardware implementation of the HIS, as detailed in the following section.

III. Continuous-Discrete Transformation

In this section, we formulate a comprehensive continuous-discrete transformation for $\boldsymbol{\rho}$, which is then applied to derive the expressions for communication and sensing SINRs. Based on this transformation, we approximate the continuous pattern design in (7) into a joint transmit-receive beamforming problem in the discrete domain.

A. Comprehensive Continuous-Discrete Transformation

Due to the continuity of pattern at HIS, we first transform patterns into discrete domains. For an integrable $\boldsymbol{\rho}$ defined over surface D , $\boldsymbol{\rho}(p)$ can be equivalently converted from the space domain into the wavenumber domain as [34]

$$\rho_i(p) = \sum_n^{\infty} w_{i,n} \Psi_n(p), \quad i = 1, \dots, K + M, \quad (8)$$

where $w_{i,n}$ is the coefficient of the i -th pattern projected to the n -th Fourier transform function $\Psi_n(p)$. By substituting (8) into (2), the electric field is represented by

$$e(p') = j\kappa Z_0 \sum_{i=1}^{K+M} \sum_n^{\infty} x_i w_{i,n} f_{2D}^n(G_{p'}) + v_c, \quad (9)$$

where $f_{2D}^n(G_{p'}) \triangleq \int_D G(p', p) \Psi_n(p) dp$ is the Green's function Fourier transform over surface D .

To overcome the integral functions in the pattern design, we provide a closed-form expression for $f_{2D}^n(G_{p'})$ in the following.

The expression of the scalar Green's function in the far-field is given by

$$G(\mathbf{r}, \mathbf{s}) = \frac{e^{j\kappa\|\mathbf{r}-\mathbf{s}\|}}{4\pi\|\mathbf{r}-\mathbf{s}\|}, \quad (10)$$

where \mathbf{r} and \mathbf{s} are positions of the point target and source, respectively. Let $\mathbf{r} = (r, \theta, \psi)$ denote the position of p' in the Spherical coordinate, and $\mathbf{s} = (s_x, s_y)$ be a source point at the surface in the Cartesian coordinate. The Euclidean distance in the Cartesian coordinate system is calculated as

$$\|\mathbf{r}-\mathbf{s}\| \approx r - \sin\theta (s_x \cos\psi + s_y \sin\psi). \quad (11)$$

By substituting (11) into (10), the Green's function on the far field is approximated as

$$G_{p'} = \frac{e^{j\kappa r}}{4\pi r} e^{-j\kappa s_x \sin\theta \cos\psi} e^{-j\kappa s_y \sin\theta \sin\psi}. \quad (12)$$

Combining (12) and (9), the Green's function Fourier transform $f_{2D}^n(G_{p'})$, is given by

$$f_{2D}^n(G_{p'}) = \int_D \frac{e^{j\kappa r}}{4\pi r} e^{-j\kappa s_x \sin\theta \cos\psi} e^{-j\kappa s_y \sin\theta \sin\psi} \Psi_n(p) dp, \quad (13)$$

where we decompose the n -th order $n = (n_x, n_y)$ along the x -axis and y -axis, the Fourier transform function $\Psi_n(p)$ is rewritten as

$$\Psi_n(p) = \frac{1}{\sqrt{A_T}} e^{-j2\pi(\frac{n_x}{L_x}(s_x - \frac{L_x}{2}))} e^{-j2\pi(\frac{n_y}{L_y}(s_y - \frac{L_y}{2}))}. \quad (14)$$

Let $\kappa_x^n = \kappa \left(\sin\theta \cos\psi + \lambda \frac{n_x}{L_x} \right)$ and $\kappa_y^n = \kappa \left(\sin\theta \sin\psi + \lambda \frac{n_y}{L_y} \right)$ denote the wavenumbers along the x -axis and y -axis, respectively. Combining (13) with (14), the closed-form Green's function Fourier transform for arbitrary position (r, θ, ψ) can be calculated by (15).

$$\begin{aligned} f_{2D}^n(G_{p'}) &= \frac{e^{j\kappa r}}{4\pi r \sqrt{A_T}} e^{j(n_x + n_y)\pi} \\ &\int_{L_x} e^{-j\kappa_x^n s_x} ds_x \int_{L_y} e^{-j\kappa_y^n s_y} ds_y \\ &= \frac{e^{j\kappa r} e^{j(n_x + n_y)\pi}}{4\pi r \sqrt{A_T}} \left[\frac{e^{-j\kappa_x^n s_x}}{-j\kappa_x^n} \right]_{-\frac{L_x}{2}}^{\frac{L_x}{2}} \left[\frac{e^{-j\kappa_y^n s_y}}{-j\kappa_y^n} \right]_{-\frac{L_y}{2}}^{\frac{L_y}{2}} \\ &= \frac{e^{j\kappa r} \sqrt{A_T}}{4\pi r} e^{j(n_x + n_y)\pi} \text{sinc}\left(\kappa_x^n \frac{L_x}{2}\right) \text{sinc}\left(\kappa_y^n \frac{L_y}{2}\right). \end{aligned} \quad (15)$$

It's obvious that $f_{2D}^n(G_{p'})$ is determined by the κ_x^n and κ_y^n . Taking the x -axis as example, when the x -axis wavenumber satisfies

$$\kappa \left(\sin\theta \cos\psi + \lambda \frac{n_x}{L_x} \right) \cdot \frac{L_x}{2} \geq n\pi, \quad (16)$$

the corresponding sinc term approaches its first zero,

indicating that higher-order terms contribute negligibly to the total response and can be safely truncated. Consequently, the truncation order (n_x, n_y) should satisfy $\{|n_x| \geq \frac{L_x}{\lambda}; |n_y| \geq \frac{L_y}{\lambda}\}$, and the minimum total truncation order is bounded by $N \geq (2\frac{L_x}{\lambda} + 1)(2\frac{L_y}{\lambda} + 1)$. It is worth clarifying that the spatial DoFs of the aperture are fundamentally determined by its electrical size [39] and do not depend on the truncation order itself. In particular, the maximum number of independent spatial DoFs supported by the continuous-aperture is bounded by $\frac{\pi A_T}{\lambda^2}$. The condition in (16) specifies a sufficient truncation order such that the retained Fourier modes fully capture the intrinsic DoFs supported by the continuous-aperture. When this condition is satisfied, higher-order terms contribute negligibly, and increasing the truncation order beyond this point does not yield additional DoFs.

B. Representation of Communication and sensing SINRs

Based on the previous transformation, the communication SINR can be described as follows. Combining (15) with (2), the received signal at user k is calculated as

$$\hat{e}_k = j\kappa Z_0 \sum_{i=1}^{K+M} \sum_n^{\infty} x_i w_{i,n} f_{2D}^n(G_k) + v_c, \quad k = 1, \dots, K. \quad (17)$$

According to [9], [34], the channel gain $\sum_n^{\infty} f_{2D}^n(G_k)$ within the band of $[-\kappa, \kappa]$ dominates the radiation power over the Fourier wavenumber domain. According to (16), the Fourier series $f_{2D}^n(G_k)$ can be approximated up to the N -th order, comprising vector

$$\mathbf{f}_k = [f_{2D}^1(G_k), \dots, f_{2D}^N(G_k)]^H, \quad k = 1, \dots, K. \quad (18)$$

For convenience, we also collect the coefficients of the i -th pattern into a vector (beamformer)

$$\mathbf{w}_i = [w_{i,1}, \dots, w_{i,N}]^H, \quad i = 1, \dots, K + M. \quad (19)$$

Then, the beamforming matrix \mathbf{W} of the whole pattern is expressed by $\mathbf{W} = [\mathbf{W}_c, \mathbf{W}_r]$, where $\mathbf{W}_c \triangleq [\mathbf{w}_1, \dots, \mathbf{w}_K]$ and $\mathbf{W}_r \triangleq [\mathbf{w}_{K+1}, \dots, \mathbf{w}_{K+M}]$ are the beamforming matrices for communication data streams and sensing streams, respectively. By combining equations (17), (18), and (19), we approximate the received signal at the k -th user as

$$\begin{aligned} \mathcal{E}_k = & j\kappa Z_0 \mathbf{f}_k^H \mathbf{w}_k c_k + \underbrace{\sum_{i=1, i \neq k}^K j\kappa Z_0 \mathbf{f}_k^H \mathbf{w}_i c_i}_{\text{Multi-user Interference}} \\ & + \underbrace{j\kappa Z_0 \mathbf{f}_k^H \mathbf{W}_r \mathbf{s}}_{\text{Sensing Interference}} + v_c, \quad k = 1, \dots, K. \end{aligned} \quad (20)$$

Therefore, combining (3) with (20), the SINR at the k -th user is expressed by (21).

Similar to the transmit end, the receive pattern in the continuous space domain is converted into the discrete Fourier domain by $\tau_l(p') = \sum_n^{\infty} q_{l,n} \Phi_n(p')$, where $q_{l,n}$ is the coefficient of the l -th receive pattern projected to $\Phi_n(p')$. We confine the Fourier series $g_{2D}^n(G_m^*)$ over surface \mathcal{P}_R to the N -th order and comprise vector $\mathbf{g}_m^* =$

$[g_{2D}^1(G_m^*), \dots, g_{2D}^N(G_m^*)]^H$. The coefficients of the l -th pattern are collected into a vector $\mathbf{q}_l = [q_{l,1}, \dots, q_{l,N}]^H$. Combining (15) with (5), the received echo w.r.t. the l -th target is approximated as

$$\begin{aligned} \mathcal{Y}_l = & \underbrace{j\kappa Z_0 \mathbf{q}_l^H \mathbf{G}_l \mathbf{W} \mathbf{x}}_{\text{Target echo}} + \underbrace{\sum_{m=1, m \neq l}^M j\kappa Z_0 \mathbf{q}_l^H \mathbf{G}_m \mathbf{W} \mathbf{x}}_{\text{Interference echo}} \\ & + \underbrace{\mathbf{q}_l^H \mathbf{v}_r}_{\text{Beamformer Noise}}, \quad l = 1, \dots, M, \end{aligned} \quad (23)$$

where $\mathbf{G}_m = \mathbf{g}_m \mathbf{g}_m^H$, and \mathbf{v}_r is the Fourier transform of v_r over surface D via the truncated order N .

Remark 1: The discrete-domain receive noise vector \mathbf{v}_r obtained via the truncated Fourier representation follows an i.i.d. circularly symmetric complex Gaussian distribution with covariance $\mathbf{v}_r \sim \mathcal{CN}(0, \sigma_r^2 \mathbf{I}_N)$.

Proof: See Appendix. A ■

Accordingly, the receive beamformer \mathbf{q}_l of the HISAC system ensures that the signal of interest is received without amplification and attenuation, allowing for accurate reception and signal processing. With unit-power beamformer \mathbf{q}_l at \mathcal{P}_R , the corresponding sensing SINR w.r.t. the l -th target in (6) is then expressed as (22).

C. Antenna Architecture

According to the continuous-discrete transformation, the HIS beam pattern can be reconstructed by summing N beams with specific wavenumbers. Consequently, the continuous beam pattern of the HIS can be effectively approximated using a discrete set of N beams. To achieve the continuous-discrete transformation of the HIS and optimize its pattern, we consider the fully-digital architecture, as shown in Fig. 3. In the following subsections, we briefly introduce the antenna architecture and discuss its corresponding beamformer models.

1) Fully-Digital Architecture: In the fully-digital antenna architecture, each beam's feed is connected to a dedicated RF chain, as shown in Fig. 3. This configuration provides the HISAC system with maximum flexibility in signal processing, allowing independent control over the patterns of each beam. Within this framework, the transmit HIS beamforming design corresponds directly to the Fourier transform coefficient matrix \mathbf{W} in (21) and (22). Similarly, the receive HIS beamforming is implemented through simultaneous reception, which aligns with the coefficient vectors \mathbf{q}_l in (22). Consequently, leveraging the principle of continuous-discrete transformation, HIS's beam can be turned by designing the \mathbf{W} matrix within the fully-digital architecture.

To implement the continuous HIS in hardware, we construct the surface using $N = N_x \times N_y$ square-shaped radiators, densely tiled to form the full aperture. Here, N_x and N_y denote the number of truncated Fourier orders along the x - and y -axes, respectively. Each radiator occupied an area of $A_T / (N_x - 1)(N_y - 1)$ serves as a sub-element that supports programmable radiation or reception characteristics. On the transmit side, the radiation

$$\eta_c(\mathbf{W}; k) = \frac{\mathbf{f}_k^H \mathbf{w}_k \mathbf{w}_k^H \mathbf{f}_k}{\mathbf{f}_k^H \mathbf{W} \mathbf{W}^H \mathbf{f}_k - \mathbf{f}_k^H \mathbf{w}_k \mathbf{w}_k^H \mathbf{f}_k + \frac{\sigma_r^2}{\kappa^2 Z_0^2}}, \quad k = 1, \dots, K. \quad (21)$$

$$\eta_r(\mathbf{W}, \mathbf{q}_l; l) = \frac{\mathbf{q}_l^H \mathbf{G}_l \mathbf{W} \mathbf{W}^H \mathbf{G}_l^H \mathbf{q}_l}{\mathbf{q}_l^H \left(\sum_{m=1}^M \mathbf{G}_m \mathbf{W} \mathbf{W}^H \mathbf{G}_m^H - \mathbf{G}_l \mathbf{W} \mathbf{W}^H \mathbf{G}_l^H \right) \mathbf{q}_l + \frac{\sigma_r^2}{\kappa^2 Z_0^2}}, \quad l = 1, \dots, M. \quad (22)$$

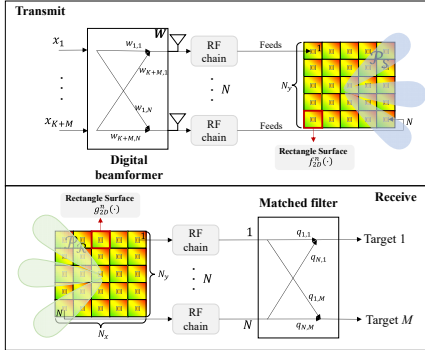


Fig. 3. The fully-digital HIS architecture.

function of each unit is operated by the basis function $f_{2D}^n(\cdot)$, while on the receive side, the directional response is represented by $g_{2D}^n(\cdot)$. The overall EM behavior of the HIS is then synthesized through the weighted superposition of these N radiators.

Unlike discrete arrays that use dipole-like isotropic radiators, HIS employs a continuous surface composed of densely packed rectangular patches to excite surface currents [13], [16], enabling enhanced beamforming control. Note that the number of RF chains in our fully-digital architecture is set to be equal to the truncation order N , ensuring one-to-one mapping between digital control and spatial basis functions. In future work, the proposed design may be extended to hybrid architectures with fewer RF chains than N , where spatial multiplexing can be achieved by phase shifters.

D. Problem Formulation in Discrete Domain

Based on the above antenna architecture, we consider beamforming matrices \mathbf{W} and \mathbf{Q} as optimization variables. From (21) and (22), both the sensing and communication SINRs are converted into the discrete domain and determined by transmit beamformers in \mathbf{W} and receive beamformers collected in $\mathbf{Q} = [\mathbf{q}_1, \dots, \mathbf{q}_M]$. The original problem in (7) is converted from the continuous domain into the discrete domain. Based on the transformation in Section III-A and truncation in Section III-B, the resulting approximated problem w.r.t. the joint transmit-receive

beamforming can be formulated as

$$\max_{\mathbf{W}, \mathbf{Q}} \min_{l=1, \dots, M} \eta_r(\mathbf{W}, \mathbf{q}_l; l), \quad (24a)$$

$$\text{s.t. } \eta_c(\mathbf{W}; k) \geq \Gamma_c, \quad k = 1, \dots, K, \quad (24b)$$

$$\|\mathbf{W}\|_F^2 \leq P_T, \quad (24c)$$

$$\|\mathbf{q}_l\|_2^2 = 1, \quad l = 1, \dots, M, \quad (24d)$$

where $\eta_r(\mathbf{W}, \mathbf{q}_l; l)$ and $\eta_c(\mathbf{W}; k)$ are defined by (22) and (21), respectively. In [16], the authors provide a methodology for computing the physical radiation power for a given surface configured by multiple patterns. The total transmit power of transmit patterns can be upper-bounded by [16]

$$\int_D \|\rho(p)\|_2^2 dp = \|\mathbf{W}\|_F^2 \leq P_T. \quad (25)$$

In (24d), the unit-power requirement for receive beamformers at \mathcal{P}_R is indicated.

Due to the non-convex max-min objective function and coupled optimized variables in objective and constraints, (24) is non-convex and challenging to solve. To circumvent the difficulties, we develop an efficient AO algorithm to address the joint transmit-receive beamforming in the HISAC system.

IV. Joint Transmit-Receive Beamforming in HISAC

In this section, we develop an AO algorithm to address the joint transmit-receive beamforming in our proposed HISAC system under fully-digital architecture. We begin with introducing the transmit HIS beamforming in Section IV-A, which we then utilize to design the receive beamforming with fixed transmit beamforming in Section IV-B. In addition, we analyze the complexity and convergence of the proposed algorithm in Section IV-C.

A. HIS Transmit Beamforming with Fixed Receive Beamforming

In this section, we optimize the transmit beamforming matrix \mathbf{W} with fixed receive beamforming matrix \mathbf{Q} . In particular, we propose a SDR-based algorithm to obtain the optimal solution of (24) iteratively. Then, we develop an ABS method to efficiently accelerate the convergence speed.

1) SDR-Based Algorithm: For the convenience of analysis, we rewrite the SINR of the sensing and communication

in terms of the covariance matrix \mathbf{R} , represented by

$$\eta_c(\mathbf{R}; k) = \frac{\mathbf{f}_k^H \mathbf{R}_k \mathbf{f}_k}{\mathbf{f}_k^H (\mathbf{R} - \mathbf{R}_k) \mathbf{f}_k + \frac{\sigma_r^2}{\kappa^2 Z_0^2}}, \quad k = 1, \dots, K,$$

$$\eta_r(\mathbf{R}; l) = \frac{\mathbf{q}_l^H \mathbf{G}_l \mathbf{R} \mathbf{G}_l^H \mathbf{q}_l}{\mathbf{q}_l^H \left(\sum_{m=1}^M \mathbf{G}_m \mathbf{R} \mathbf{G}_m^H - \mathbf{G}_l \mathbf{R} \mathbf{G}_l^H \right) \mathbf{q}_l + \frac{\sigma_r^2}{\kappa^2 Z_0^2}},$$

$$l = 1, \dots, M, \quad (26)$$

where $\mathbf{R}_k = \mathbf{w}_k \mathbf{w}_k^H$ and $\mathbf{R} = \mathbf{W} \mathbf{W}^H$. With the given receive beamformer $\mathbf{Q} = [\mathbf{q}_1, \dots, \mathbf{q}_M]$, we propose to maximize the minimal sensing SINR by optimizing the total covariance matrix \mathbf{R} and its sub-element \mathbf{R}_k .

To deal with it, we first omit the rank-one constraints and transform (24) into a series of feasibility-checking [40] sub-problems by SDR as

$$\max_{\mathbf{R}, \mathbf{R}_1, \dots, \mathbf{R}_K, \Gamma_r} \Gamma_r, \quad (27a)$$

$$\text{s.t. } \eta_r(\mathbf{R}; l) \geq \Gamma_r, \quad l = 1, \dots, M, \quad (27b)$$

$$\eta_c(\mathbf{R}; k) \geq \Gamma_c, \quad k = 1, \dots, K, \quad (27c)$$

$$\mathbf{R} \succeq 0, \quad (27d)$$

$$\mathbf{R}_k \succeq 0, \quad k = 1, \dots, K, \quad (27e)$$

$$\mathbf{R} - \sum_{k=1}^K \mathbf{R}_k \succeq 0, \quad (27f)$$

$$\text{tr}(\mathbf{R}) \leq P_T, \quad (27g)$$

where Γ_r is an auxiliary variable to replace the minimal sensing SINR in the objective function.

Due to the fractional terms in constraints (27b) and (27c), the above problem is still non-convex. Let $\mathbf{U}_{l,m} = \mathbf{G}_m^H \mathbf{q}_l \mathbf{q}_l^H \mathbf{G}_m$, $\mathbf{F}_k = \mathbf{f}_k \mathbf{f}_k^H$. By fixing Γ_r and rearranging (27b) and (27c) as

$$(1 + \Gamma_r^{-1}) \text{tr}(\mathbf{U}_{l,l} \mathbf{R}) - \sum_{m=1}^M \text{tr}(\mathbf{U}_{l,m} \mathbf{R}) \geq \frac{\sigma_r^2}{\kappa^2 Z_0^2}, \quad (28)$$

and

$$(1 + \Gamma_c^{-1}) \text{tr}(\mathbf{F}_k \mathbf{R}_k) - \text{tr}(\mathbf{F}_k \mathbf{R}) \geq \frac{\sigma_c^2}{\kappa^2 Z_0^2}, \quad (29)$$

respectively. (27) becomes a convex semidefinite programming (SDP) feasibility-checking problem and can be solved by off-the-shelf toolbox such as CVX [41]. By providing a potential range for Γ_r that contains the optimal Γ_r^* , (27) can be solved by checking its feasibility with Γ_r being chosen in a bisection manner. Specifically, we perform a bisection search over the interval $[\Gamma_{r,start}, \Gamma_{r,end}]$, as shown in Algorithm 1.

Let $\hat{\mathbf{R}}_1, \dots, \hat{\mathbf{R}}_K, \hat{\mathbf{R}}$ be the optimal solution of (27), each entry of the communication beamforming matrix $\hat{\mathbf{W}}_c$ is calculated by

$$\hat{\mathbf{w}}_k = \left(\mathbf{f}_k^H \hat{\mathbf{R}}_k \mathbf{f}_k \right)^{-\frac{1}{2}} \hat{\mathbf{R}}_k \mathbf{f}_k, \quad k = 1, \dots, K, \quad (30)$$

and the beamforming matrix $\hat{\mathbf{W}}_r$ for multi-target sensing

Algorithm 1 Bisection Search with SDR

Input: Γ_c .

- 1: Determine $\Gamma_{r,start} = 0$, $\Gamma_{r,end} = \frac{\kappa^2 Z_0^2 P_T A_T}{\sigma_r^2}$.
 - 2: repeat
 - 3: Update $\Gamma_r \leftarrow \frac{1}{2} (\Gamma_{r,start} + \Gamma_{r,end})$.
 - 4: Solve (27) by checking its feasibility with Γ_r . If (27) is feasible, $\Gamma_{r,start} \leftarrow \Gamma_r$; otherwise $\Gamma_{r,end} \leftarrow \Gamma_r$.
 - 5: until $\Gamma_{r,end} - \Gamma_{r,start} \leq \epsilon_1$
 - 6: Update the minimal sensing SINR as $\Gamma_{r,start}$.
 - 7: Calculate $\mathbf{R}, \mathbf{R}_1, \dots, \mathbf{R}_K$ by solving (27) with $\Gamma_{r,start}$.
- Output: $\mathbf{R}, \mathbf{R}_1, \dots, \mathbf{R}_K$.
-

is choosing by

$$\hat{\mathbf{W}}_r \hat{\mathbf{W}}_r^H = \hat{\mathbf{R}} - \sum_{k=1}^K \hat{\mathbf{R}}_k. \quad (31)$$

The optimal solution $\bar{\mathbf{R}}_1, \dots, \bar{\mathbf{R}}_K$ for (24) is reconstructed as $\bar{\mathbf{R}}_k = \hat{\mathbf{w}}_k \hat{\mathbf{w}}_k^H$, for $k = 1, \dots, K$, which is exactly rank-one and optimal.

It is noteworthy that, for different HISAC system setups, the dynamic searching range for potential values of feasible Γ_r changes rapidly, leading to high overhead. To overcome this challenge, we propose an ABS method which is detailed in the following, which provides a refined/shrunk searching range for Γ_r to accelerate the convergence of Algorithm 1.

2) Adaptive Bisection Searching Method: The main concept of ABS is to find a smaller range for feasible Γ_r , thereby accelerating convergence. For convenience, we rewrite the constraint (28) with an indicator t , given by

$$(1 + \Gamma_r^{-1}) \text{tr}(\mathbf{U}_{l,l} \mathbf{R}) - \sum_{m=1}^M \text{tr}(\mathbf{U}_{l,m} \mathbf{R}) - \sigma_R^2 \geq t, \quad (32)$$

where the equivalent noise is represented by $\sigma_R^2 = \frac{\sigma_r^2}{\kappa^2 Z_0^2}$. The objective function in (27) is then converted into finding the maximal t under the fixed Γ_r , which satisfies the inequality in (32). Subsequently, we employ the indicator t to evaluate the feasibility of the given Γ_r for the problem (27).

First, for the initial point of the ABS, we define the maximal potential value of the Γ_r as $\Gamma_{r,start}$, satisfying

$$\Gamma_{r,start} = \frac{P_T A_T}{\sigma_R^2} - K \Gamma_c, \quad (33)$$

where $\frac{P_T A_T}{\sigma_R^2}$ is the system's upper bound in the absence of interference-noise, and $K \Gamma_c$ is interference from the multi-user communication. Given $\Gamma_{r,start}$, (27) can be solved with SDPt3 [41], and the indicator t is computed by (32). Intuitively, when $t \geq 0$, the actual lower bound of the feasibility solution surpasses the given $\Gamma_{r,start}$, whereas when $t \leq 0$, the actual lower bound of the feasibility solution falls below the given $\Gamma_{r,start}$. Consequently, with the guidance of t , a refined range for Γ_r can be obtained by iteratively modifying the initial $\Gamma_{r,start}$ with steps $\Gamma_{r,start} \rightarrow \Gamma_{r,start} - \Gamma_c$.

Algorithm 2 Adaptive Bisection Searching Method

Input: Γ_c .Initial point: $\Gamma_{r,start} = \frac{P_T A_T}{\sigma_R^2} - K\Gamma_c$.

1: while 1 do

2: Compute the indicator t with fixed $\Gamma_{r,start}$ via (32).3: If $t \geq 0$, break; otherwise $\Gamma_{r,start} \leftarrow \Gamma_{r,start} - \Gamma_c$.

4: end while

5: $\Gamma_{r,end} \leftarrow \Gamma_{r,start} + \Gamma_c$.

6: while 1 do

7: Compute the indicator t with fixed $\Gamma_{r,end}$ via (32).8: If $t \leq 0$, break; otherwise $\Gamma_{r,end} \leftarrow \Gamma_{r,end} + \Gamma_c$.

9: end while

10: $\Gamma_{r,start} \leftarrow \Gamma_{r,end} - \Gamma_c$.Output: $[\Gamma_{r,start}, \Gamma_{r,end}]$.

In addition, we define the end point of the potential range as $\Gamma_{r,end} = \Gamma_{r,start} + \Gamma_c$, which should be checked with indicator t . Similar to the initial point modification, when $t \geq 0$, the actual upper bound of the feasibility solution surpasses the given $\Gamma_{r,end}$, indicating that $\Gamma_{r,end} \rightarrow \Gamma_{r,end} + \Gamma_c$. After multiple iterations, we obtain the refined dynamic searching range for Γ_r , denoted as $[\Gamma_{r,start}, \Gamma_{r,end}]$. The detailed steps of ABS are summarized in Algorithm 2.

Finally, combined with a confined searching range obtained by the proposed ABS approach, the SDR-based bisection method in Algorithm 1 is employed to calculate the solution to the problem (27), with t serving as the solution indicator. Once the search range meets $\Gamma_{r,end} - \Gamma_{r,start} \leq \epsilon_1$ and $t \geq 0$, the iterative algorithm ends to obtain the optimal solution $\mathbf{R}, \mathbf{R}_1, \dots, \mathbf{R}_K$, which we then utilize to calculate the transmit beamformer \mathbf{W} via (30) and (31).

B. HIS Receive Beamforming with Fixed Transmit Beamforming

For a given transmit beamforming matrix \mathbf{W} , in order to maximize the minimal sensing SINR among all targets, (24) is converted to

$$\max_{\mathbf{Q}} \min_{l=1, \dots, M} \eta_r(\mathbf{q}_l; l), \quad (34a)$$

$$\text{s.t. } \|\mathbf{q}_l\|_2^2 = 1, l = 1, \dots, M. \quad (34b)$$

The receive beamforming design is still non-convex due to the fractional terms in the objective function. To tackle this problem, we propose a generalized Rayleigh quotient-based method.

First, since the optimization for each receive beamformer \mathbf{q}_l w.r.t. the l -th target is independent of sensing SINR of other targets, (34) can be decoupled into M sub-problems, i.e.,

$$\max_{\mathbf{q}_l} \frac{\mathbf{q}_l^H \mathbf{A}_l \mathbf{q}_l}{\mathbf{q}_l^H (\mathbf{A} - \mathbf{A}_l) \mathbf{q}_l + \frac{\sigma_r^2}{\kappa^2 Z_0^2}}, \quad (35a)$$

$$\text{s.t. } \|\mathbf{q}_l\|_2^2 = 1, \quad (35b)$$

where $\mathbf{A}_l = \mathbf{G}_l \mathbf{W} \mathbf{W}^H \mathbf{G}_l^H$ and $\mathbf{A} = \sum_{m=1}^M \mathbf{G}_m \mathbf{W} \mathbf{W}^H \mathbf{G}_m^H$. Then, we have the following lemma based on the generalized Rayleigh quotient [42], [43].

Lemma 1: The objective function in problem (35) can be equivalently written as

$$\max_{\mathbf{q}_l} \frac{\mathbf{q}_l^H \mathbf{B} \mathbf{q}_l}{\mathbf{q}_l^H \mathbf{C} \mathbf{q}_l}, \quad (36)$$

where $\mathbf{B} = \mathbf{A}_l$ and $\mathbf{C} = \mathbf{A} - \mathbf{A}_l + \mathbf{I} \frac{\sigma_r^2}{\kappa^2 Z_0^2}$. It is obvious that, for any given beamformer \mathbf{q}_l , we have the following results: $\mathbf{q}_l^H \mathbf{B} \mathbf{q}_l \geq 0$, $\mathbf{q}_l^H \mathbf{C} \mathbf{q}_l > 0$. Therefore, $\mathbf{B} \succeq 0$ and $\mathbf{C} \succ 0$ are positive semidefinite and positive definite matrices, respectively. Further, both \mathbf{B} and \mathbf{C} are apparently Hermitian matrices, thereby converting problem (35) into a generalized Rayleigh quotient maximization problem (36). Based on the Rayleigh quotient theory [42], [43], the optimal solution of (36) is given by

$$\mathbf{C}^{-1} \mathbf{B} \mathbf{v} = \lambda_{max} (\mathbf{C}^{-1} \mathbf{B}) \mathbf{v}, \quad (37)$$

where $\lambda_{max} (\mathbf{C}^{-1} \mathbf{B})$ is the maximal eigenvalue of $\mathbf{C}^{-1} \mathbf{B}$, and \mathbf{v} is the corresponding eigenvector.

Based on Lemma 1, the optimal receive beamformer \mathbf{q}_l is given by \mathbf{v} . The corresponding sensing SINR is $\lambda_{max} (\mathbf{C}^{-1} \mathbf{B})$.

We summarize the entire process of the proposed AO-based joint transmit-receive beamforming for HISAC system in Algorithm 3.

Algorithm 3 AO-Based Joint Transmit-Receive Beamforming for HISAC System

Input: Γ_c .

1: repeat

2: Determine $(\Gamma_{r,start}, \Gamma_{r,end})$ via Algorithm 2.

3: repeat

4: Update $\mathbf{R}, \mathbf{R}_1, \dots, \mathbf{R}_K$ via Algorithm 1.5: until $\Gamma_{r,end} - \Gamma_{r,start} \leq \epsilon_1$ 6: Update \mathbf{W} via (30) and (31).7: Update \mathbf{q}_l via (37).8: Update the minimal sensing SINR Γ_r^* .9: Update $\Gamma_{r,start} \leftarrow \Gamma_r^*$.10: until $\left| \Gamma_r^{*(i)} - \Gamma_r^{*(i-1)} \right| < \epsilon_2$ Output: \mathbf{W}, \mathbf{Q} .

Specifically, the transmit beamformers and receive beamformers are updated alternately until a given convergence tolerance between two iterative steps is met, i.e., $\left| \Gamma_r^{*(i)} - \Gamma_r^{*(i-1)} \right| < \epsilon_2$, where $\Gamma_r^{*(i)}$ and $\Gamma_r^{*(i-1)}$ denote the minimal sensing SINR in (i) -th and $(i-1)$ -th iterations, respectively.

C. Complexity and Convergence Analysis

1) Computational Complexity Analysis: The computational complexity of the proposed AO algorithm comprises two parts: transmit-side optimization and receive-side update. The transmit-side optimization is formulated as

an SDP, whose complexity dominates the overall computation. The receive-side update reduces to a generalized Rayleigh quotient problem and admits a closed-form solution. Consequently, each iteration of the proposed algorithm involves solving an SDP and then performing a closed-form update. In the following, we provide the computational complexity of each sub-algorithm.

- Optimization of transmit beamforming matrices \mathbf{W}_c , \mathbf{w}_r with fixed receive HIS configuration: The SDP problem in (26) is solved by the ABS-SDR approach. Specifically, given the potential values of Γ_r , the number of execution steps of the ABS I_o . Given the solution accuracy ϵ_1 , the complexity of using the SDR to solve (26) is $\mathcal{O}(N^{3.5} \log(1/\epsilon_1))$ [44]. Therefore, the computational complexity of transmit beamforming algorithm is $I_o \times \mathcal{O}(N^{3.5} \log(1/\epsilon_1))$.
- Optimization of receive HIS configuration with fixed transmit beamforming matrices: Since we suggest the generalized Rayleigh quotient algorithm to address (35), the complexity of this algorithm is $\mathcal{O}(N^3)$.

As a result, the computational complexity of the proposed alternating algorithm for each iteration is $I_o \times \mathcal{O}(N^{3.5} \log(1/\epsilon_1)) + \mathcal{O}(N^3)$.

2) Convergence Analysis: Due to the non-convex nature of the joint transmit-receive beamforming problem, global optimality of Algorithm 3 cannot be formally guaranteed. However, the proposed AO algorithm ensures convergence to a stationary point, as each subproblem yields either a convex formulation or a closed-form solution, and guarantees that the objective value does not decrease in each iteration. On the receiver side, the HIS configuration is optimized using a generalized Rayleigh quotient, which yields a closed-form solution without iterative updates. Therefore, convergence analysis primarily focuses on the transmit-side HIS optimization and the overall AO process. For the transmit-side configuration, we adopt an adaptive algorithm based on the SDR framework, termed ABS-SDR. The algorithm iteratively adjusts the search interval $[\Gamma_{r,start}, \Gamma_{r,end}]$ according to the achieved sensing SINR. If the SINR improves, the new configuration is accepted and the search region is tightened. Otherwise, the algorithm reverts to the previous configuration. Since both sensing and communication SINR are inherently bounded due to physical limitations such as total transmit power, this ascent property guarantees the convergence of the ABS-SDR algorithm. As both subproblems exhibit the ascent property and are constrained within a limited power constraint, the overall AO algorithm is guaranteed to converge.

V. Numerical Results

In this section, we provide numerical results to evaluate the performance of our proposed HISAC system and validate the effectiveness of the proposed algorithms.

A. Simulation Setup

Without specified otherwise, the simulation parameters are summarized in Table II, and the geometry of the

simulation scenario is illustrated in Fig. 4. The \mathcal{P}_S and \mathcal{P}_R

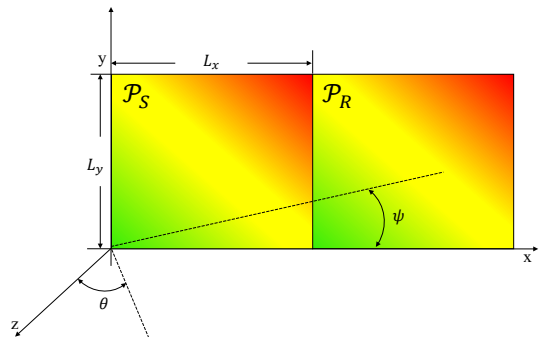


Fig. 4. Illustration of the proposed HISAC simulation scenario.

are located in the XOY plane adjacently. Simultaneously, all communication users and radar targets are located on the far-field radiation region of the HIS, represented by polar coordinates. Additionally, to underscore the superiority of the proposed HISAC system, we utilize the discrete array counterpart, where antennas are deployed with half-wavelength spacing, as a baseline. Note that the transmit power P_T is computed based on the continuous-aperture current model, where the unit is expressed in mA^2 rather than in watt [16]. Moreover, the truncation order is not optimized on a per-scenario basis. Instead, it is determined by the physical aperture size and the carrier wavelength, which jointly limit the wavenumber bandwidth of the radiated field. Once the aperture is fixed, the truncation order can be selected according to (16), and remains unchanged across various communication and sensing scenarios.

TABLE II
The basic simulation parameters

Parameters	Value
Center frequency	2.4 GHz
Aperture size	$A_T = 0.5 \times 0.5 \text{ m}^2$
Transmit power budget	$P_T = 100 \text{ mA}^2$
Position of the 1-th user	$(30^\circ, 180^\circ)$
Position of the 2-th user	$(30^\circ, 270^\circ)$
Position of the target 1	$(30^\circ, 90^\circ)$
Position of the target 2	$(30^\circ, 45^\circ)$
Γ_c	5 dB

Remark 2: Compared to the HIS, we assume the discrete-array-based system consists of discrete patches (isotropic source) with half-wavelength inter-distance. The aperture size of the discrete array remains the same as the HIS, allowing $D = Dx Dy = \frac{L_x}{\lambda/2} \frac{L_y}{\lambda/2}$ antennas to be optimized. According to [45], the efficient aperture size of the isotropic source is given by $e_a = \frac{\lambda^2}{4\pi}$. Therefore, the maximal radiation power of the discrete array with

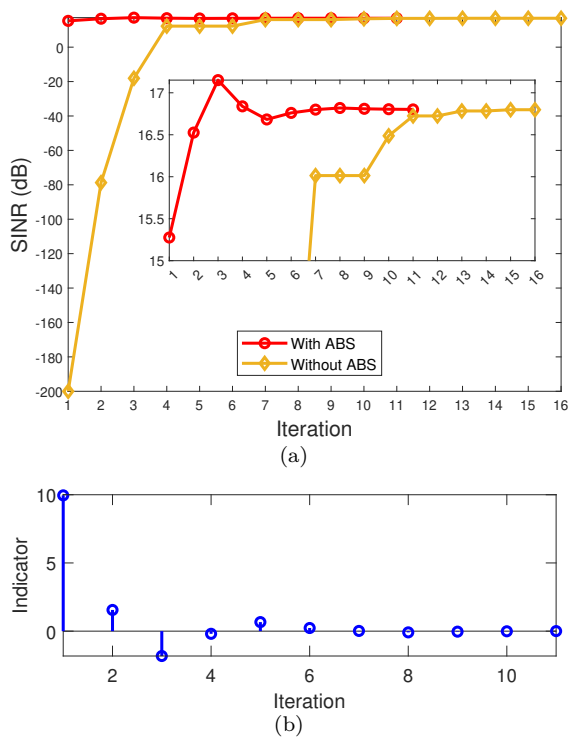


Fig. 5. Illustration of algorithm convergence. (a) Convergence of Algorithm 1 with ABS and without ABS. (b) Convergence of the indicator t .

D elements can be calculated as $\frac{P_T A_T}{\pi}$. Based on this setup, compared to the HISAC system, the round-trip performance degradation of the discrete array counterpart is $\left(\frac{c_a D}{L_x L_y}\right)^2 = \frac{1}{\pi^2}$.

B. Performance Evaluation

1) **Algorithm Convergence:** First, we study the convergence of the AO-based approach in Algorithm 3 and the SDR-based method in Algorithm 1 with ABS acceleration in Algorithm 2. In particular, Algorithm 3 converges within two steps, demonstrating its efficacy and robustness. Fig. 5(a) presents the convergence trends of the SDR-based method with ABS and without ABS acceleration. We can see that, with the proposed ABS in Algorithm 2, the search range of Γ_r is shrunk, accelerating the convergence of the SDR-based bisection search in Algorithm 1. Specifically, under a given convergence tolerance, the proposed algorithm converges within 11 steps, while the algorithm without ABS requires another 6 steps to reach its convergence. To evaluate the impact of the indicator t on the proposed algorithm's convergence, Fig. 5(b) shows the convergence trend of the indicator t . As can be seen, the indicator t converges to 0, implying the optimal solution to (27) is found. Specifically, when $t > 0$, the potential value Γ_r is feasible but not optimal; when $t < 0$, the potential value Γ_r is infeasible. If and only if $t \rightarrow 0$, the solution of (27) converges to the optimal value. Therefore, the minimal sensing SINR oscillates and converges to the maximal value after multiple iterations.

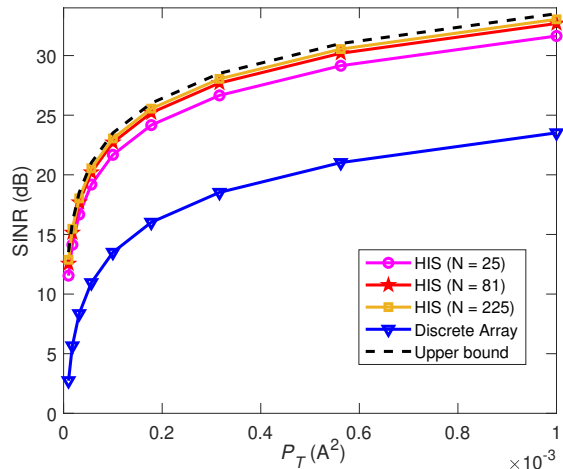


Fig. 6. Sensing SINR versus the power budget P_T .

2) **Multi-User Single-Target Scenario:** We evaluate the performance gain of our proposed HISAC system with its discrete array counterpart and verify the effectiveness of the AO algorithm by visualizing the transmit beams. For comparison, the upper bound of sensing performance in the HISAC system is defined as the sensing SINR without communication interference, which can be calculated by $\frac{P_T A_T}{\sigma_R^2}$ via (33).

In Fig. 6, we evaluate the sensing SINR versus the maximal transmit power P_T for different ISAC configurations. We observe that our proposed HISAC system outperforms the discrete array counterpart in the considered range of power budget. Moreover, with sufficiently large transmit power, the proposed system exhibits a 9.5 dB sensing SINR improvement compared to the discrete-array-based ISAC system. The reason is that, under the same physical aperture size, the efficient size of the discrete array is smaller than that of HIS, leading to insufficient power radiation and receiving. As stated in Remark 2, the round-trip radiation power degradation compared to HIS is π^2 , resulting in the sensing SINR undergoing 9.94 dB. Therefore, with the fulfilling capture of the HIS radiation, the performance gain of the HISAC system compared to the discrete array will stabilize around $\pi^2 \rightarrow 9.94$ dB.

To explore the impact of aperture size on the HISAC system, we evaluate the sensing SINR versus the aperture area A_T in Fig. 7, where the transmit HIS always remains a square with $L_x = L_y = \sqrt{A_T}$. As can be seen, the radar performance improves with the increase of the aperture size, and the sensing SINR of our proposed HISAC system exhibits a progressive enhancement as the Fourier expansion order N increases, outperforming its discrete array counterpart even when N is moderately large. However, if the Fourier expansion order is too small to adequately capture the HIS radiation characteristics, the radar performance degrades significantly in the large-aperture region and may fall below that of the discrete array counterpart.

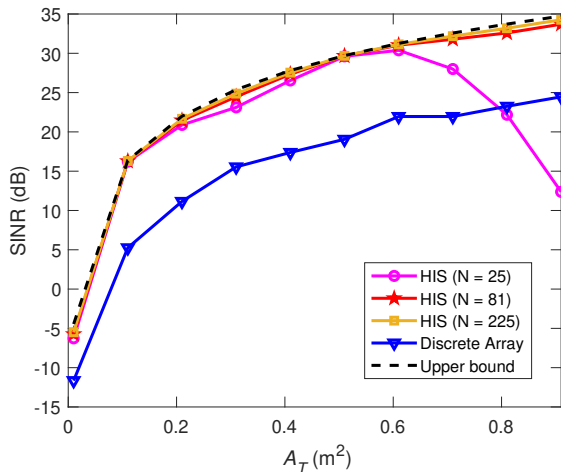


Fig. 7. Sensing SINR versus the aperture size A_T of the transmit HIS.

In Fig. 8(a) and Fig. 8(b), we illustrate the transmit and receive beampatterns of the HIS and that of the discrete array at $\theta = 30^\circ$ plane, respectively. Based on these normalized beampatterns, we study the beampattern gain between the HIS-based and discrete-array-based system. As can be seen, in the transmit phase, as the Fourier expansion order N increases, the beamwidth of the HIS's transmit beampattern tightens, where the peak power reaches its maximum until the N is sufficient for characterizing the HIS radiation. Meanwhile, the peak value of the transmit beampattern based on the discrete array demonstrates 4.9 dB degradation compared to HIS, which agrees with π . In addition, for the receive beampattern w.r.t. target 1, the peak value of the HIS's beampattern outperforms that of the discrete array with a 9.7 dB enhancement. As a result, the sensing SINR for target 1 can be significantly improved after the receive beamforming under the proposed HISAC transceiver architecture. The reason is that both the HIS's transmit and receive beamformers are optimized at the receiver side, leading to the overall sensing SINR improvement in our proposed architecture.

In Fig. 9, we explore the sensing SINR under varying communication SINR requirements. Specifically, we evaluate sensing SINR versus different communication threshold Γ_c . The physical aperture size is $A_T = 0.6 \times 0.6 \text{ m}^2$ to demonstrate the superior sensing SINR difference between Fourier expansion order N and its discrete array counterpart. A clear trade-off between sensing and communication is presented, in which the sensing SINR decreases as the communication SINR requirement increases. In addition, we observe that our proposed HISAC system shows robustness compared to the discrete array system, possessing more significant sensing performance gain with higher communication SINR threshold. Specifically, as Γ_c increases, the sensing SINR gain of the HISAC system over the discrete array-based ISAC system increases from 7.4 dB to 15.6 dB, demonstrating the advantages of

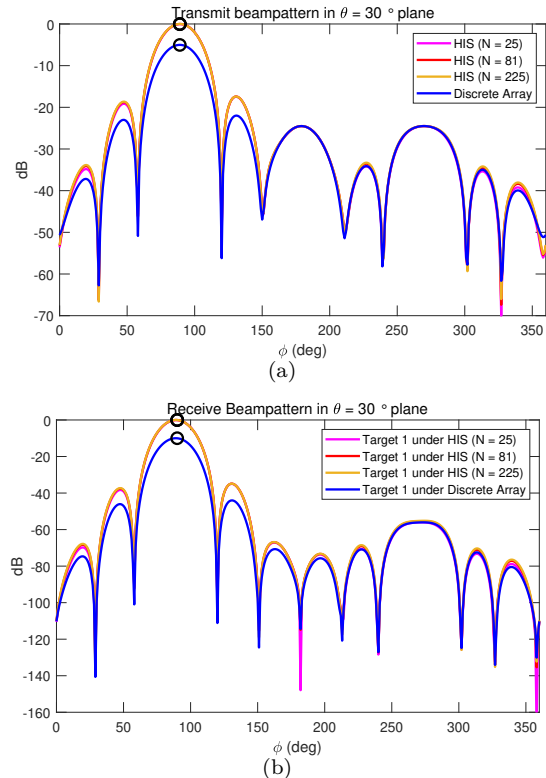


Fig. 8. HIS beampatterns for target 1. (a) Transmit beampattern. (b) Receive beampattern.

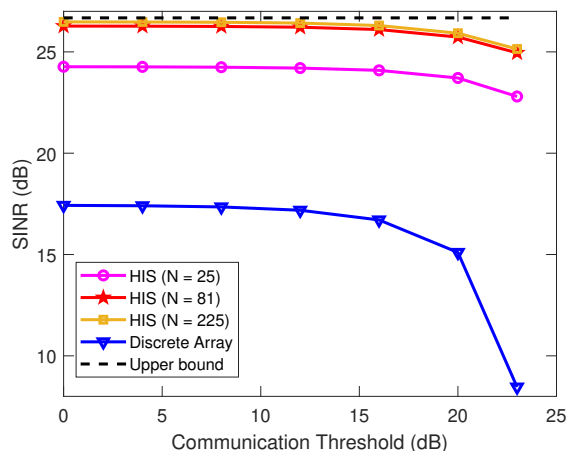


Fig. 9. Sensing SINR versus communication SINR threshold Γ_c .

incorporating HIS into ISAC systems.

3) Multi-User Multi-Target Scenario: To evaluate the scalability and effectiveness of the proposed HISAC framework, we provide comprehensive simulations under a multi-user and multi-target scenario. An additional radar target positioned at $(30^\circ, 45^\circ)$ is introduced in the multi-user multi-target scenario. In Fig. 10, we compare the minimal sensing SINR among radar targets for different Fourier expansion order N versus P_T . As observed, due to inter-target interference, the sensing SINR undergoes a 3 dB degradation, compared to the interference-free upper bound. Nevertheless, our proposed HISAC system still

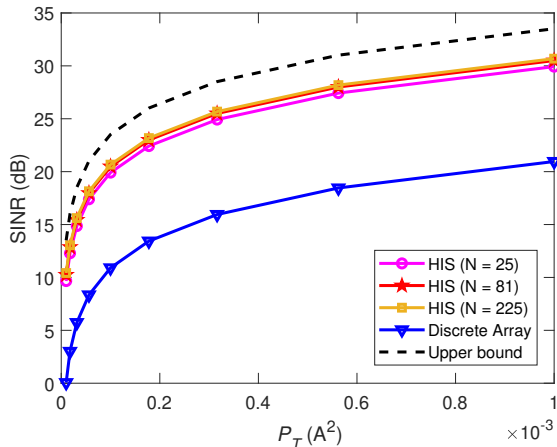


Fig. 10. Minimal sensing SINR versus the power budget P_T .

outperforms its discrete array counterpart with 9.7 dB sensing SINR enhancement. The insight here is that the number of radar targets will not affect the sensing SINR enhancement between the HIS and the discrete array. This is because the radiation power of both architectures is independent of the number/directions of targets. Therefore, when the Fourier expansion order N is sufficient, our system can still achieve power gain around π^2 .

In Fig. 11, we illustrate the normalized transmit and receive beampatterns at $\theta = 30^\circ$ plane to demonstrate the impact of multi-target sensing on the minimal sensing SINR. As observed in Fig. 11(a), the main lobe of the HIS transmit beampattern is split into two main lobes with the same peak level. Compared to the discrete array, the transmit beampattern of HIS exhibits a 4.9 dB enhancement in each direction of targets. As can be seen in Fig. 11(b), the receiving beamforming strengthens the beampattern's peak values in the directions of targets while suppressing those of the clutters (targets located in other directions) deeply. Specifically, for the receive beamforming w.r.t. target 1, the direction w.r.t. target 1 is enhanced while the direction w.r.t. target 2 is suppressed and vice versa. Note that the peak value of HIS still maintains an enhancement around 9.7 dB compared to the discrete array, regardless of the directions of the receive beamforming. Therefore, our proposed algorithm is efficient in addressing the multi-user multi-target scenario and indicates that the sensing SINR improvement is attributed to the efficient aperture and is independent of the directions of targets.

To further evaluate the robustness of the proposed HISAC system under channel uncertainty, we conduct simulations under imperfect CSI conditions. The angular deviation Δ_θ represents the mismatch between the estimated and actual angle of arrival/departure for User 1, thereby capturing CSI inaccuracy. We compare the sensing and communication SINR across all radar targets and communication users for both HIS-based and discrete-array-based systems. As shown in Fig. 12, the results reveal a distinct trade-off between the Fourier

truncation order N of the HIS and its robustness to CSI error. Specifically, higher-order HIS configurations achieve better radiation fidelity and stronger beamforming gain under ideal CSI, but become more sensitive to imperfect CSI. Nevertheless, all HIS configurations consistently outperform their discrete-array-based counterparts, even under moderate CSI error. Results demonstrate that the efficient aperture utilization of HIS enables stable SINR performance for both sensing and communication tasks.

VI. Conclusion and Discussion

This paper introduced a novel concept to ISAC systems by proposing the HISAC system. Through the continuous-aperture array fabrication of both transmitter and receiver, the HISAC system presented unique challenges in design. To address these, we developed a Fourier-based continuous-discrete transformation that maps the continuous pattern into a finite-dimensional wavenumber domain, enabling compatibility with traditional discrete-array ISAC frameworks. Based on this reformulation, a joint transmit-receive beamforming problem was formulated to balance multi-target sensing performance with multi-user communication requirements. An AO-based algorithm was developed to efficiently tackle the non-convex optimization with coupled variables. Numerical results demonstrated superior performance compared to traditional discrete-array-based ISAC systems, achieving significantly enhanced sensing capabilities while maintaining predetermined communication performance levels.

A. Discussion

1) **Hardware Implementation Challenges in HIS Systems:** This work focuses on the algorithmic and theoretical modeling of continuous-aperture HIS. However, practical implementation introduces several hardware-level challenges that must be addressed before real-world deployment. The proposed HISAC framework assumes a fully-digital HIS architecture, in which each beam, corresponding to a Fourier-domain coefficient, is driven by a dedicated RF chain. However, implementing such a system in practice entails significant hardware complexity, particularly due to the delicate RF chains. To bridge the gap between theoretical models and practical systems, future implementations may consider hybrid HIS architectures, which offer a trade-off between flexibility and complexity. In addition, hardware imperfections such as phase quantization, nonlinearities, and finite control resolution should be carefully modeled to understand their impact on system performance. These non-idealities primarily distort the effective HIS beampattern and can be incorporated into the proposed framework through uncertainty-aware constraints or robust optimization formulations.

2) **Scalability in Multi-HIS and Large-Scale Networks:** The proposed HISAC system already adopts a dual-HIS configuration, in which separate transmit and receive HISs are deployed to support full-duplex ISAC functionality. However, extending the framework to cell-free MIMO

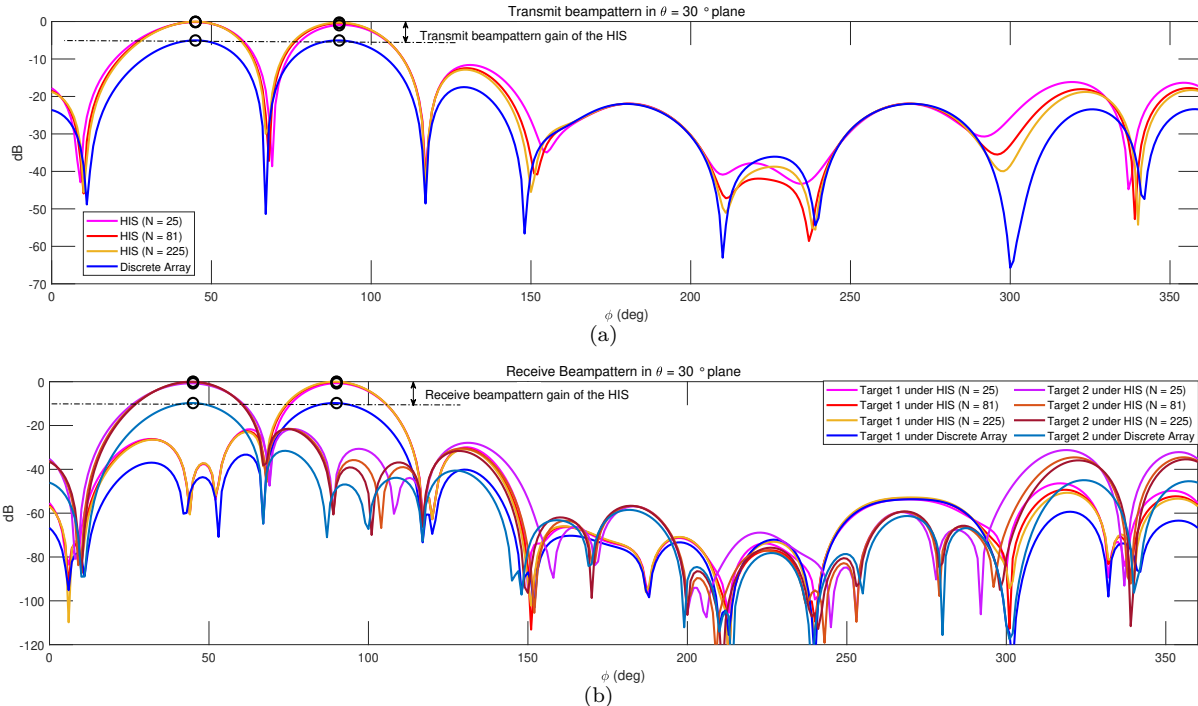


Fig. 11. HIS beampatterns for multi-target. (a) Transmit beampattern. (b) Receive beampattern.

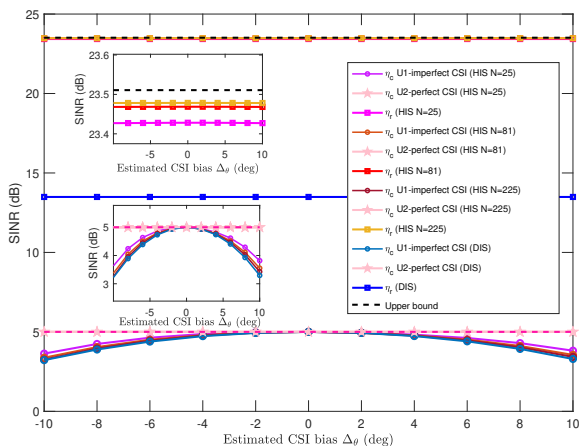


Fig. 12. SINRs for sensing and communication versus imperfect CSI bias.

or multistatic sensing, which requires the cooperation among multiple base stations/HISs, has yet to be explored. In such distributed settings, inter-HIS synchronization, mutual interference suppression, and coordinated beam scheduling become essential. As the number of cooperative HIS nodes increases, the dimensionality of control variables grows accordingly, which substantially increases the computational complexity of joint optimization. For large-scale deployments involving multiple HISs, future research may investigate low-rank structural modeling, learning-assisted beam coordination strategies, and distributed optimization algorithms. These approaches can facilitate scalable and adaptive system operation while maintaining global performance constraints.

3) System-Level Design Based on the HIS representation: Under dual-HIS full-duplex operation, SI arises from spectral coupling between transmit and receive excitations, which is typically overlooked in conventional ISAC studies. Although the proposed Fourier-domain representation provides a promising framework for characterizing such coupling, its integration with dedicated SI suppression mechanisms remains an open problem. Moreover, the current ISAC signal model is formulated based on stochastic signal design via covariance optimization. Extending this framework toward deterministic sensing waveform design is another important direction for future investigation. At the system level, additional performance metrics, such as communication capacity, energy efficiency, and real-time computational latency, will also be explored to achieve a more comprehensive evaluation of practical performance.

Appendix

A. Proof of Remark 1

We now justify the i.i.d. Gaussian model adopted in the discrete domain. Specifically, we assume the receive-side noise is a spatially white circularly symmetric complex Gaussian random field satisfying [34]

$$\mathbf{E}(v_r(p')v_r^*(p'')) = \sigma_r^2\delta(p' - p''), \quad p', p'' \in D, \quad (\text{A.1})$$

where $\delta(\cdot)$ is the Dirac delta function. Let $\{\Phi_n(p')\}_{n=1}^N$ be the truncated orthonormal Fourier basis. The n -th Fourier coefficient of the noise is defined as

$$v_{r,n} = \int_D v_r(p')\Phi_n(p')dp', \quad n = 1, \dots, N. \quad (\text{A.2})$$

Collecting $v_{r,n}$ into vector \mathbf{v}_r , with the the orthogonality of $\Phi_n(\cdot)$, we obtain

$$\begin{aligned} \mathbf{E}(\mathbf{v}_r \mathbf{v}_r^H) &= \\ & \left[\int_D \int_D \mathbf{E}(v_r(p') v_r^*(p'') \Phi_n(p') \Phi_n^*(p'')) dp' dp'' \right]_{n,n'} \quad (\text{A.3}) \\ &= \sigma_r^2 \mathbf{I}_N. \end{aligned}$$

Therefore, $\mathbf{v}_r \sim \mathcal{CN}(0, \sigma_r^2 \mathbf{I}_N)$, which validates the noise model in (23).

This concludes the proof.

References

- [1] J. A. Zhang, F. Liu, C. Masouros, R. W. Heath, Z. Feng, L. Zheng, and A. Petropulu, "An overview of signal processing techniques for joint communication and radar sensing," *IEEE Journal of Selected Topics in Signal Processing*, vol. 15, no. 6, pp. 1295–1315, Nov 2021.
- [2] F. Liu, Y. Cui, C. Masouros, J. Xu, T. X. Han, Y. C. Eldar, and S. Buzzi, "Integrated sensing and communications: Toward dual-functional wireless networks for 6G and beyond," *IEEE Journal on Selected Areas in Communications*, vol. 40, no. 6, pp. 1728–1767, Jun 2022.
- [3] X. Liu, T. Huang, N. Shlezinger, Y. Liu, J. Zhou, and Y. C. Eldar, "Joint transmit beamforming for multiuser MIMO communications and MIMO radar," *IEEE Transactions on Signal Processing*, vol. 68, pp. 3929–3944, Jun 2020.
- [4] H. Hua, J. Xu, and T. X. Han, "Optimal transmit beamforming for integrated sensing and communication," *IEEE Transactions on Vehicular Technology*, vol. 72, no. 8, pp. 10 588–10 603, Mar 2023.
- [5] Z. He, W. Xu, H. Shen, Y. Huang, and H. Xiao, "Energy efficient beamforming optimization for integrated sensing and communication," *IEEE Wireless Communications Letters*, vol. 11, no. 7, pp. 1374–1378, Apr 2022.
- [6] J. Wang, S. Gong, Q. Wu, and S. Ma, "RIS-aided MIMO systems with hardware impairments: Robust beamforming design and analysis," *IEEE Transactions on Wireless Communications*, vol. 22, no. 10, pp. 6914–6929, Feb 2023.
- [7] L. Chen, Z. Wang, Y. Du, Y. Chen, and F. R. Yu, "Generalized transceiver beamforming for DFRC with MIMO radar and MU-MIMO communication," *IEEE Journal on Selected Areas in Communications*, vol. 40, no. 6, pp. 1795–1808, Mar 2022.
- [8] F. Liu, Y.-F. Liu, A. Li, C. Masouros, and Y. C. Eldar, "Cramér-rao bound optimization for joint radar-communication beamforming," *IEEE Transactions on Signal Processing*, vol. 70, pp. 240–253, Dec 2021.
- [9] O. T. Demir, E. Björnson, and L. Sanguinetti, "Channel modeling and channel estimation for holographic massive MIMO with planar arrays," *IEEE Wireless Communications Letters*, vol. 11, no. 5, pp. 997–1001, Feb 2022.
- [10] R. Deng, Y. Zhang, H. Zhang, B. Di, H. Zhang, H. V. Poor, and L. Song, "Reconfigurable holographic surfaces for ultra-massive MIMO in 6G: Practical design, optimization and implementation," *IEEE Journal on Selected Areas in Communications*, vol. 41, no. 8, pp. 2367–2379, Jun 2023.
- [11] F. Liu and C. Masouros, "Hybrid beamforming with sub-arrayed MIMO radar: Enabling joint sensing and communication at mmwave band," in *ICASSP 2019-2019 IEEE International Conference on Acoustics, Speech and Signal Processing (ICASSP)*. IEEE, May 2019, pp. 7770–7774.
- [12] G. Gradoni and M. Di Renzo, "End-to-end mutual coupling aware communication model for reconfigurable intelligent surfaces: An electromagnetic-compliant approach based on mutual impedances," *IEEE Wireless Communications Letters*, vol. 10, no. 5, pp. 938–942, Jan 2021.
- [13] A. Pizzo, L. Sanguinetti, and T. L. Marzetta, "Fourier plane-wave series expansion for holographic MIMO communications," *IEEE Transactions on Wireless Communications*, vol. 21, no. 9, pp. 6890–6905, Mar 2022.
- [14] A. Pizzo, T. L. Marzetta, and L. Sanguinetti, "Spatially-stationary model for holographic MIMO small-scale fading," *IEEE Journal on Selected Areas in Communications*, vol. 38, no. 9, pp. 1964–1979, Jun 2020.
- [15] M. A. Jensen and J. W. Wallace, "Capacity of the continuous-space electromagnetic channel," *IEEE Transactions on Antennas and Propagation*, vol. 56, no. 2, pp. 524–531, Feb 2008.
- [16] Z. Zhang and L. Dai, "Pattern-division multiplexing for multi-user continuous-aperture MIMO," *IEEE Journal on Selected Areas in Communications*, vol. 41, no. 8, pp. 2350–2366, Jun 2023.
- [17] H. Zhang, H. Zhang, B. Di, M. D. Renzo, Z. Han, H. V. Poor, and L. Song, "Holographic integrated sensing and communication," *IEEE Journal on Selected Areas in Communications*, vol. 40, no. 7, pp. 2114–2130, Mar 2022.
- [18] R. Deng, Y. Zhang, H. Zhang, B. Di, H. Zhang, and L. Song, "Reconfigurable holographic surface: A new paradigm to implement holographic radio," *IEEE Vehicular Technology Magazine*, vol. 18, no. 1, pp. 20–28, Jan 2023.
- [19] L. Wei, C. Huang, G. C. Alexandropoulos, E. Wei, Z. Zhang, M. Debbah, and C. Yuen, "Multi-user holographic MIMO surfaces: Channel modeling and spectral efficiency analysis," *IEEE Journal of Selected Topics in Signal Processing*, vol. 16, no. 5, pp. 1112–1124, May 2022.
- [20] S. Hu, F. Rusek, and O. Edfors, "Beyond massive MIMO: The potential of data transmission with large intelligent surfaces," *IEEE Transactions on Signal Processing*, vol. 66, no. 10, pp. 2746–2758, Mar 2018.
- [21] C. Huang, S. Hu, G. C. Alexandropoulos, A. Zappone, C. Yuen, R. Zhang, M. Di Renzo, and M. Debbah, "Holographic MIMO surfaces for 6G wireless networks: Opportunities, challenges, and trends," *IEEE wireless communications*, vol. 27, no. 5, pp. 118–125, Jul 2020.
- [22] J. Pritzker, J. Ward, and Y. C. Eldar, "Transmit precoder design approaches for dual-function radar-communication systems," *arXiv preprint arXiv:2203.09571*, Mar 2022.
- [23] C. Wen, Y. Huang, and T. N. Davidson, "Efficient transceiver design for MIMO dual-function radar-communication systems," *IEEE Transactions on Signal Processing*, vol. 71, pp. 1786–1801, May 2023.
- [24] Z. Liu, H. Zhang, T. Huang, F. Xu, and Y. C. Eldar, "Hybrid RIS-assisted MIMO dual-function radar-communication system," *IEEE Transactions on Signal Processing*, vol. 72, pp. 1650–1665, Feb 2024.
- [25] Y. Zhang, W. Ni, J. Wang, W. Tang, M. Jia, Y. C. Eldar, and D. Niyato, "Robust transceiver design for covert integrated sensing and communications with imperfect CSI," *IEEE Transactions on Communications*, pp. 1–1, Apr 2024.
- [26] M. Cao, X. Liu, H. Zhang, Y. C. Eldar, and H. Zhang, "Hybrid near-field and far-field localization with holographic MIMO," *IEEE Transactions on Wireless Communications*, vol. 25, pp. 10 560–10 575, Jan 2026.
- [27] Q. Huang, Y. Zhao, J. Hu, K. Yang, and Y. Fang, "Circular holographic MIMO beamforming for integrated data and energy multicast systems," *IEEE Transactions on Wireless Communications*, vol. 25, pp. 5733–5748, Oct 2025.
- [28] B. Di, H. Zhang, Z. Han, R. Zhang, and L. Song, "Reconfigurable holographic surface: A new paradigm for ultra-massive mimo," *IEEE Transactions on Cognitive Communications and Networking*, vol. 11, no. 6, pp. 3761–3783, Mar 2025.
- [29] J. Jalali, M. Darabi, and R. C. de Lamare, "Shape adaptive reconfigurable holographic surfaces," in *2025 IEEE 102nd Vehicular Technology Conference (VTC2025-Fall)*, Oct 2025, pp. 1–5.
- [30] H. Zhang, H. Zhang, B. Di, and L. Song, "Holographic integrated sensing and communications: Principles, technology, and implementation," *IEEE Communications Magazine*, vol. 61, no. 5, pp. 83–89, Feb 2023.
- [31] J. Zhu, Z. Wan, L. Dai, M. Debbah, and H. V. Poor, "Electromagnetic information theory: Fundamentals, modeling, applications, and open problems," *IEEE Wireless Communications*, vol. 31, no. 3, pp. 156–162, Jan 2024.
- [32] R. Deng, B. Di, H. Zhang, D. Niyato, Z. Han, H. V. Poor, and L. Song, "Reconfigurable holographic surfaces for future wireless communications," *IEEE Wireless Communications*, vol. 28, no. 6, pp. 126–131, Jan 2022.

- [33] T. Gong, P. Gavrilidis, R. Ji, C. Huang, G. C. Alexandropoulos, L. Wei, Z. Zhang, M. Debbah, H. V. Poor, and C. Yuen, "Holographic MIMO communications: Theoretical foundations, enabling technologies, and future directions," *IEEE Communications Surveys & Tutorials*, vol. 26, no. 1, pp. 196–257, Aug 2023.
- [34] L. Sanguinetti, A. A. D'Amico, and M. Debbah, "Wavenumber-division multiplexing in line-of-sight holographic MIMO communications," *IEEE Transactions on Wireless Communications*, vol. 22, no. 4, pp. 2186–2201, Feb 2022.
- [35] Z. Wan, J. Zhu, Z. Zhang, L. Dai, and C.-B. Chae, "Mutual information for electromagnetic information theory based on random fields," *IEEE Transactions on Communications*, vol. 71, no. 4, pp. 1982–1996, Feb 2023.
- [36] M. Karimipour, N. Komjani, and I. Aryanian, "Shaping electromagnetic waves with flexible and continuous control of the beam directions using holography and convolution theorem," *Scientific reports*, vol. 9, no. 1, p. 11825, 2019.
- [37] A. Sabharwal, P. Schniter, D. Guo, D. W. Bliss, S. Rangarajan, and R. Wichman, "In-band full-duplex wireless: Challenges and opportunities," *IEEE Journal on Selected Areas in Communications*, vol. 32, no. 9, pp. 1637–1652, Jun 2014.
- [38] R. Liu, M. Li, Y. Liu, Q. Wu, and Q. Liu, "Joint transmit waveform and passive beamforming design for RIS-aided DFRC systems," *IEEE Journal of Selected Topics in Signal Processing*, vol. 16, no. 5, pp. 995–1010, May 2022.
- [39] D. Dardari, "Communicating with large intelligent surfaces: Fundamental limits and models," *IEEE Journal on Selected Areas in Communications*, vol. 38, no. 11, pp. 2526–2537, Jul 2020.
- [40] L. Zhang, R. Zhang, Y.-C. Liang, Y. Xin, and S. Cui, "On the relationship between the multi-antenna secrecy communications and cognitive radio communications," *IEEE Transactions on Communications*, vol. 58, no. 6, pp. 1877–1886, Jun 2010.
- [41] K.-C. Toh, M. J. Todd, and R. H. Tütüncü, "SDPT3—a MATLAB software package for semidefinite programming, version 1.3," *Optimization methods and software*, vol. 11, no. 1-4, pp. 545–581, Jan 1999.
- [42] X. Wang, Z. Fei, and Q. Wu, "Integrated sensing and communication for RIS-assisted backscatter systems," *IEEE Internet of Things Journal*, vol. 10, no. 15, pp. 13 716–13 726, Mar 2023.
- [43] M. Zhang, Y. He, Y. Cai, G. Yu, and N. Al-Dhahir, "Design and performance analysis of wireless legitimate surveillance systems with radar function," *IEEE Transactions on Communications*, vol. 71, no. 4, pp. 2517–2531, Feb 2023.
- [44] Z.-Q. Luo, W.-K. Ma, A. M.-C. So, Y. Ye, and S. Zhang, "Semidefinite relaxation of quadratic optimization problems," *IEEE Signal Processing Magazine*, vol. 27, no. 3, pp. 20–34, 2010.
- [45] C. A. Balanis, *Antenna theory: analysis and design*. John wiley & sons, Feb 2016.